Electrical conductivity properties of porous $SmBaCo_2O_{5+d}$ and $SmBa_{0.5}Sr_{0.5}Co_2O_{5+d}$ layered perovskite oxide systems for solid oxide fuel cell

Kyeong Eun Song [a], Harald Schlegl [b], Chan Gyu Kim [a], Ki Sang Baek [a], Yu Ri Lim [a], Jung Hyun Nam [c], Hyun-Suk Kim [d], Jung Hyun Kim [a, *]

[a] Department of Advanced Materials Science and Engineering, Hanbat National University, 125, Dongseo-Daero, Yuseong-Gu, Daejeon, 34158, Republic of Korea

[b] Chemistry Department, Lancaster University, Bailrigg, Lancaster LA1 4YB, United Kingdom

[c] Department of Polymer Science and Engineering, Sungkyunkwan University, Suwon 16419, Republic of Korea

[d] Department of Materials Science and Engineering, Chungnam National University, Daejeon, 34134, Republic of Korea

Corresponding author:*

Jung Hyun Kim: jhkim2011@hanbat.ac.kr, jhkim1870@gmail.com,

Tel: +82-42-821-1239, Fax: +82-42-821-1592,

Department of Advanced Materials Science and Engineering, Hanbat National University, 125, Dongseo-Daero, Yuseong-Gu, Daejeon, 34158, Republic of Korea

Abstract

In this study, the electrical conductivity characteristics of $SmBaCo_2O_{5+d}$ (SBCO) and $SmBa_{0.5}Sr_{0.5}Co_2O_{5+d}$ (SBSCO) were measured and analyzed by changing the characteristics of the microstructure from dense microstructure to porous microstructure for the cathode application in solid oxide fuel cells. SBCO and SBSCO comprised of the dense microstructure showed metal insulator transition (MIT) and metallic behavior, respectively. In SBCO, when the oxygen partial pressure is reduced, the conductivity value decreases, and the conductivity behavior changes to the behavior of a semiconductor. However, the electrical conductivity behavior of SBSCO did not change even when the oxygen partial pressure was decreased. The electrical conductivities of the porous cathodes were lower than those of the dense cathodes due to the discontinuous electric path, but all porous cathodes showed semiconductor behavior. The conductivity value decreases when the oxygen partial pressure decreases, but the general conductivity behavior of the samples with a porous microstructure does not change under N_2 atmosphere. The porous cathode showed the highest electrical conductivity when Pt lines were led to the top of the cathode. In this case, a relatively high electrical conductivity was measured using the method of measuring multiple conductivities at different temperatures while decreasing the measurement temperature starting from a high temperature rather than the method of measuring while raising the temperature starting from a low temperature. In the dense cathode, higher electrical conductivities were measured when a low current was applied, but in the porous cathode, the same electrical conductivity values were measured regardless of the applied current values.

Keywords: Cathode, Electrical Conductivity, Porous microstructure, Dense microstructure.

Highlight

● All porous cathodes were shown to display semiconductor conductivity behavior.

● The electrical conductivity of the sample in which the Pt line was printed on the cathode surface was the highest.

● Dense cathodes have higher electrical conductivity when a low current is applied.

● Porous cathodes have no difference in electrical conductivity with respect to the applied current value.

1. Introduction

A Solid Oxide Fuel Cell (SOFC) is an energy device that generates electrical energy directly from the chemical energy of oxygen and hydrogen [1]. The temperature characteristics operating in the high temperature ranges (600 ~ 1000 ºC) improve the power density of SOFC and show the advantage of high efficiency compared to other fuel cells [2, 3]. However, the high operation temperature does not only work as an advantage, but rather may also have a disadvantageous effect. For example, during operation, problems such as the chemical reaction between constituents, deterioration, Cr poisoning, and metal oxidation occur [4, 5].

To solve these problems, research and development on Intermediate Temperature-operating Solid Oxide Fuel Cells (IT-SOFCs) is being conducted, which has recently successfully demonstrated operation at a lower operating temperature of 500 ~ 800 ºC. An IT-SOFC cell is basically composed of cathode, anode and electrolyte. Among these units of electrodes and electrolyte, the cathode is responsible for about 50 % of total polarization resistance, so it is an important factor determining the performance of the SOFC [6]. However, since an IT-SOFC operates at a relatively low temperature, the cathode performance reduction problems such as slow oxygen reduction reaction (ORR) and activation loss occur to an even higher degree than at a high temperature SOFC [7-9]. For this reason, recently many researchers have actively been conducting research on the cathode with stable and high-performance characteristics [10-12].

Conductivity is a factor representing the electrochemical properties of the cathode. The conductivity of a cathode refers to the degree to which an electric current can pass easily and an electric charge can be carried. The total conductivity (σ_{total}) is the sum of the conductivity by charge carriers such as electrons or holes ($\sigma_{electron}$) and the conductivity by ions (σ_{ion}) as shown in Equation 1 below.

$$\sigma_{Total} = \sigma_{electron} + \sigma_{ion} + \sigma_{etc} \quad \text{(Equation 1)}$$

When the cathode has superior electrical and ionic conductivities, the oxygen reduction reaction (ORR) can easily occur on the entire surface of the cathode, which results in enhanced electrochemical properties of the cathode itself and of the whole single cell. The electrical conductivity of the cathode is generally measured through a sample with a dense microstructure pressed into a bar-shape. Table 1 summarizes the electrical conductivities of various cathode materials reported recently by applying this method. [13-21].

Many researchers have reported on various cathodes showing excellent electrical conductivity using dense samples, but the cathodes for the actual SOFC are formed in the form of porous thick film for maximal active triple phase boundary (TPB) length, maximization of mass transport, and diffusion of gas [22-26]. In other words, although the electrical conductivity measured using a general measurement method is measured in a cathode with dense microstructure, there is a problem that it is different from the electrical conductivity characteristic of the typically porous cathode of an actual SOFC cell [27, 28]. Therefore, in order to compare and evaluate the electrical conductivity of the cathode used in an actual SOFC, a porous microstructural cathode should be used. In this study, $SmBaCo_2O_{5+d}$ (SBCO) and $SmBa_{0.5}Sr_{0.5}Co_2O_{5+d}$ (SBSCO) layered perovskite oxide systems, which have been reported to show excellent performance [29, 30], were fabricated into porous microstructures using screen printing, and their electrical conductivity was measured to compare with the conductivity of dense microstructure samples.

2. Experimental

2. 1. Powder preparation and X-ray Diffraction (XRD) measurement

Sm_2O_3 (Alfa Aesar), $BaCO_3$ (Alfa Aesar), $SrCO_3$ (Samchun chemicals), and Co_3O_4 (Alfa

Aesar) powders were used for the synthesis of SBCO and SBSCO by using solid state reaction (SSR). After each powder was precisely weighed according to its chemical composition, and then uniformly mixed using an agate mortar with a pestle and ethanol. The mixtures were placed in an oven and maintained at 78 °C for 24 hours to evaporate the ethanol and calcined for 6 hours at 1000 ^{o}C in air atmosphere as a first calcination step. After that, the materials were crushed, dried in an oven, and then secondary calcined for 8 hours at 1100 ^{o}C in air atmosphere to complete the final SBCO and SBSCO layered perovskite oxide systems.

XRD patterns of SBCO and SBSCO powders were obtained on a Model D/Max 2500, Rigaku (45Kv, 200 mA, Cu kα radiation); the obtained data were matched with reference data for the phase synthesis and analyzed using the MDI JADE 6 program.

2. 2. Sample preparation with dense microstructure

The SBCO and SBSCO pellets for the measurement of electrical conductivity were prepared by pressing 2 x 10^3 kg/m^2 of rectangular-shaped metal bars (25 mm x 6 mm x 4 mm). After that, the pellets were sintered at 1100 ^{o}C for 3 hours to make sample bars with a dense microstructure. The abbreviations for each dense sample were summarized in Table 2.

2. 3. Sample preparation with porous microstructure

Porous cathodes have structural characteristics that make self-sustaining impossible because of the thin thickness (within 40 micrometers in thickness). Therefore, it is necessary to measure the conductivity by coating it on electrolyte. Therefore, $Ce_{0.9}Gd_{0.1}O_{2-d}$ (CGO91) powders were pressed at 1.5 x 10^3 kg/m^2 into rectangular-shaped metal molds (30 mm x 23 mm x 2 mm) showing an aspect ratio lower than 1 for the electrolyte substrates and sintered at 1450 ^{o}C for

6 hours in air atmosphere to complete a CGO91 pellet.

For the cathode inks, SBCO and SBSCO powders were put in a Nalgene bottle with a dispersant (KD-1) and acetone, respectively, and ball milled for 24 hours. Then, it was mixed with the binder system vehicle and stirred at room temperature. The SBCO and SBSCO inks were applied to the CGO91 pellets using screen printing to fabricate porous microstructural cathodes, these samples were heat-treated at 1000 ºC for 1 hour.

Pt paste (Ferro) was used as an electrical conductor for electrical conductivity measurement. Pt paste was screen-printed on the cathode in the form of 4 probes to form Pt line circuits to apply current and voltage. In order to compare the electrical conductivity characteristics according to the location of the Pt line and the cathode, various positions of Pt line were printed. For example, when the Pt lines were on the surface of the cathode, it was named as the upper conductor (H). The middle conductor (M) sample was prepared in a form in which the Pt lines were placed between the cathode layers. The lower conductor (L) sample was prepared by depositing 4 Pt lines directly onto the electrolyte, and then screen printing the cathode paste twice on top of the Pt lines. Schematic diagrams and abbreviations of H, M and L samples were summarized in Fig. 1 and Table 3.

2. 4. Electrical conductivity analysis

The electrical conductivities of porous and dense samples were measured using DC 4 probe method by connecting sample to Keithley 2400 source meter using Pt clamp and Pt wires. The conductivity measurements were performed at temperatures between 50 ºC and 900 ºC in increments of 50 ºC. Two series of conductivity measurements were performed, one starting measurements at 50 ºC heating up to 900 ºC (Heating cycle in air) and immediately afterwards

starting measurements at 900 ºC decreasing the temperature to 50 ºC (Cooling cycle in air) in air atmosphere.

N_2 gas was fed into the quartz tube to generate low oxygen partial pressure. The electrical conductivity under N_2 condition was measured through the same method as measured in air atmosphere by first increasing the temperature from 50 to 900 ºC (Heating cycle in N_2) and subsequently decreasing the temperature from 900 to 50 ºC (Cooling cycle in N_2).

Currents of 0.05, 0.075, 0.1 and 0.3 A were applied in the air atmosphere. However, currents of 0.01, 0.02, 0.03, 0.04 and 0.05 A were applied in the N_2 atmosphere to measure the electrical conductivity. The reason for the difference in applied current was because porous cathodes were destroyed by overvoltage when the same currents as that in air atmosphere were applied in N_2 atmosphere, so the lower current applied in N_2 atmosphere.

2. 5. Microstructure analysis

The microstructures of the samples were observed at an acceleration voltage of 10 kV using a Scanning Electron Microscope (SEM, Model: HITACHI SU-5000). In addition, the microstructural properties, particle sizes and porosities were analyzed using ImageJ software.

3. Results and discussions

3. 1. Electrical conductivities of dense microstructure samples

3. 1. 1. Electrical conductivities according to heating and cooling cycles

X-ray diffraction (XRD) results of SBCO (A) and SBSCO (B) are shown in Fig. 2. After confirming that the XRD results of Fig. 2 are in good agreement with XRD results reported of

SBCO and SBSCO by our group as a single phase [31-33], the electrical conductivity was measured.

The results of electrical conductivity of D-A and D-B in air atmosphere are shown in Fig. 3 with black scatter plots (heating cycle in air, ■), and with white scatter plots (cooling cycle in air, □). According to Fig. 3. (a), D-A showed a typical metal insulator transition (MIT) behavior, in which the electrical conductivity increases with increasing temperature at lower temperature ranges and decreases with increasing temperature at a higher temperature range under both experimental conditions of heating cycle and cooling cycle in air [34]. It can be seen in Fig. 3. (b) that D-B showed metallic behavior in which the electrical conductivity decreases with increasing temperature at the experimental condition of heating and cooling cycles in air [32]. There were no differences between the conductivity behaviors and values at the condition of heating and cooling cycles in air. Numerically, D-A shows electrical conductivities of 1181.8 and 1157.2 S/cm at 100 ºC and 438.3 and 428.8 S/cm at 700 ºC measured during the heating cycle and the cooling cycle in air respectively, as shown in Fig. 3. (a). D-B shows electrical conductivities of 1216.8 and 1222.8 S/cm at 100 ºC and 355.7 and 357.5 S/cm at 700 ºC measured during heating and cooling cycles in air respectively, as shown in Fig. 3. (b). Through these measurement results, it can be seen that the electrical conductivity behavior of dense cathodes does not change depending on the measurements performed during the heating or the cooling cycles in air and there is no marked differences of the values. This is because the thermal stability was maintained during the thermal cycling of dense samples [35]. The characteristic of maintaining the same electrical conductivity in D-A and D-B from heating or cooling cycles in air indicates that these cathodes are thermally stable without phase transitions as long as they are dense without pores. In summary, the dense samples have no hysteresis characteristics of electrical conductivity at the condition of heating and cooling cycles in air.

3. 1. 2. Electrical conductivities at reduced oxygen partial pressure

The red scatter plots (■) displayed in Fig. 3 indicate the electrical conductivity results of D-A and D-B in heating cycle in N_2, and can be compared with the conductivity in heating cycle in air (■). The curves for D-A and D-B show that the conductivity measured during heating cycle in N_2 is lower than that measured during the heating cycle in air. For example, D-A in Fig. 3. (a) showed values of 1073.0 and 152.7 S/cm at 300 ºC during the heating cycle in air and N_2 respectively. In addition, D-B in Fig. 3. (b) showed values of 867.3 and 515.7 S/cm at 300 ºC during the heating cycle in air and N_2. Since D-A and D-B are p-type conductors, the electrical conductivity decreases as the oxygen partial pressure decreases. This behavior is typically found in perovskites in which Co is substituted at the B-site [36].

Also, the conductivity behavior under atmospheres with different oxygen partial pressures changed with the composition of the p-type conductor. The electrical conductivity behavior of D-A was MIT in air atmosphere but changed to semiconductor behavior in N_2 atmosphere [34, 37, 38]. However, as shown in Fig. 3. (b), D-B showed metallic conductivity behavior both under air and N_2 atmosphere. The only difference was the electrical conductivity values, which were generally higher at a higher oxygen partial pressure but there was no difference in the electrical conductivity behavior. The reason for the change in conductivity behavior in D-B could be understood as follows. Generally heating cycles and contact to reducing atmosphere with the related low oxygen partial pressure change the bonding strength between the different atoms in SBCO. A decomposition of the surface in contact with the N_2 atmosphere occurs leading to a loss of thermal stability. In SBCO, this leads to both a decrease in electrical conductivity values and to a complete change of the electrical conductivity behavior in N_2 atmosphere. In D-B, the phenomenon of surface decomposition occurred as well, but to a lesser

extent. Conductivity values of D-B decreased in low oxygen partial pressure, but the metallic behavior was maintained because the changes in the surface composition were not severe enough to change the behavior [38, 41].

3. 2. Electrical conductivities of porous microstructure samples

3. 2. 1. Electrical conductivities according to microstructural change

As mentioned in Chapter 1, the conductivity measurement of dense samples can only provide an incomplete picture about the performance of the cathode material. Under fuel cell operation conditions, the porous structure of electrodes is essential. In Fig. 3, electrical conductivity results of porous cathodes were summarized in the closed blue and pink scatter plots (■, ■). The H samples with the Pt probes located on cathode surface showed higher conductivity than samples with the Pt probes embedded inside the cathodes (M) or between electrolyte and cathode (L). For this reason, only the results of the H samples were included in Figures 3. (a) and (b). The porous SBCO and SBSCO samples show lower electrical conductivity at the same measurement conditions compared to dense cathodes in Fig. 3. For example, H-BG, which has the highest electrical conductivity among porous cathode samples, showed value of 221.5 S/cm at 700 ^{o}C respectively at the condition of heating cycle in air, as shown in Fig. 3. (b). That is, the electrical conductivities of the porous samples at the same measurement condition were lower than those of the dense samples in section 3.2.1. This is because the electrical conductivity of the porous cathode, which is a p-type conductor, is decreased by the limitation of the movement of the hole, which is the main charge carrier.

In addition, dense SBCO and SBSCO showed different conductivity behaviors such as MIT and metallic in air atmosphere, but all porous cathodes showed semiconductor behavior in

which the electrical conductivity increases with increasing temperature despite the changes in composition [34, 36-38]. In other words, when the microstructure is changed from dense to porous even for the same cathode material, the electrical conductivity value and behavior change, and the porous samples show semiconductor behavior regardless of the cathode material or compositions at all atmospheric conditions. When the oxygen partial pressure decreases by supplying N_2 gas, the electrical conductivity behavior of D-A changes from MIT to Semiconductor behavior, but the porous sample does not. That is, the electrical conductivity behavior of the porous cathode is not affected by the oxygen partial pressure.

3. 2. 2. Electrical conductivities according to the location of Pt lines

The electrical conductivities of the porous cathodes at the condition of heating and cooling cycles in air and N_2 atmosphere were summarized in Fig. 4. The H sample showed excellent electrical conductivity compared to the M and L samples under IT-SOFC operating temperature range in Figures 4. (a) ~ (d). In particular, the H-BG sample showed the highest electrical conductivity compared to all other porous samples at all measurement conditions. These results are related to the leakage current. When measuring the electrical conductivity, the method used is to measure the voltage, which is the electrochemical potential generated by the current flowing on the surface. If any leakage current into the inside of the cathode and the electrolyte under the cathode layer occurs, the movement of charge carriers can be limited. In the case of H, the amount of leakage current into the cathode and the electrolyte is smaller than that of M and L because the Pt paste, which is a conductor for applying current and measuring voltage, is on the surface. Therefore, the H samples show superior electrical conductivity because the electron conductivity in these samples is less limited [40].

3. 2. 3. Electrical conductivities according to oxygen partial pressure

Comparing the electrical conductivities at the experimental condition of heating cycle in air (■) and heating cycle in N_2 (■) from Figures 4. (a) and (c), the electrical conductivities of all porous samples were higher in the air atmosphere than N_2 atmosphere in all temperature ranges. This can be analyzed as follows through the conductivity results of H, M and L samples from Figures 4. (a) and (c).

First, the electrical conductivities of H-BG were 136.7 and 221.6 S/cm at 300 and 700 ºC in the heating cycle in air, and 109.6 and 175.0 S/cm in the heating cycle in N_2 at the same temperature. Second, M-BG showed conductivities of 27.7 and 50.1 S/cm at 300 and 700 ºC in the heating cycle in air, and 15.1 and 42.0 S/cm at the same temperatures in the heating cycle in N_2. Finally, in the case of L-BG, the conductivities were 47.1 and 84.9 S/cm at 300 and 700 ºC in the heating cycle in air, and 42.9 and 77.4 S/cm at the same temperatures in the heating cycle in N_2. As this result, the electrical conductivity showed higher value in air atmosphere.

Summarizing these results, it can be seen that in both the dense and the porous samples in Figures 3 and 4, higher oxygen partial pressure always leads to higher electrical conductivity, caused by an increase in the concentration of holes under oxidizing atmosphere, which are the conduction carriers in p-type semiconductors [41]. Therefore, when linking the results of electrical conductivity in terms of dense or porous microstructures, the electrical characteristics of the p-type conductor are maintained.

3. 2. 4. Electrical conductivities according to heating and cooling cycles

Fig. 5 summarizes the electrical conductivity values of H-BG, which has the highest electrical conductivity among all porous cathodes. The porous cathode shows difference in

electrical conductivity between heating cycle (■) and cooling cycle (□) in the air atmosphere, in contrast to the dense cathode. In particular, it can be seen that H-BG showed higher conductivity values during cooling cycle than during heating cycle. For example, the values of H-BG at heating cycle and cooling cycle in air were 223.1 and 236.8 S/cm respectively at 700 ºC with applied current of 0.1A, so the electrical conductivity was higher at the cooling cycle. This is because, when measuring while lowering the temperature after reaching the highest measured temperature (cooling cycle), the thermal activation of the porous cathode is already sufficiently achieved, and thus the charge carrier mobility present in the cathode is easier than during the heating cycle [41].

3. 2. 5. Electrical conductivities according to applied currents

The characteristics of H-BG according to the applied currents at heating and cooling cycles in air and N_2 were summarized in Fig. 6. It has been reported that in dense layered perovskite cathode samples in which Co is substituted into the perovskite B-site an increase in electrical conductivity can be achieved if a low current is applied [29, 30]. However, the porous cathodes display almost the same electrical conductivity values regardless of the applied currents. For example, the conductivities of H-BG in Fig. 6. (a) were 221.5, 223.1, 223.1 and 223.3 S/cm with applied currents of 0.05, 0.075, 0.1 and 0.3 A respectively at 750 ºC in heating cycle in air, which are almost identical values. In summary, when the microstructure of the cathode is dense, the electrical conductivity is greatly affected by the applied current, and on the other hand when the microstructure of the cathode is porous, it is not affected by the applied current.

3. 2. 6. Small polaron conduction in porous cathodes

The activation energy (Ea) of dense and porous cathodes was calculated using Equation 2 using the slope of the conductivity graphs in temperature range between 400 and 650 ºC, which showed a linear electrical conductivity in all samples: A is a material constant containing the carrier concentration term; Ea is the activation energy for hopping conduction; k is the Boltzmann's constant; T is the absolute temperature [42, 43].

$$\sigma = \frac{A}{kT}\exp(-\frac{Ea}{kT}) \qquad \text{(Equation 2)}$$

Since the porous cathodes had little difference of the electrical conductivity value by applying various currents, the T_{max} was calculated using conductivities when 0.05 A current was applied using Equation 3 and shown in Table 4 [42, 43].

$$T_{max} = \frac{Ea}{k} \qquad \text{(Equation 3)}$$

The calculated T_{max} in Table 4 is higher than the actual T_{max} (600 ~ 900 ºC) in Fig. 4 of the porous microstructure. In other words, it implies that there are other factors for reducing electrical conductivity in addition to small polaron hopping in the high-temperature range. This is due to an increase in oxygen vacancies as the amount of oxygen loss in the oxide increases at high temperatures [42, 43]. Accordingly, the electrical conductivities of all porous samples in Fig. 4 increase linearly at the medium/low temperature ranges, and although there is a difference in the exact temperature of the turning point for each sample, the electrical conductivity decreases in the high temperature range. It can be concluded that the electrical conductivity decreased because oxygen vacancies increased at high temperature ranges. Table 5 shows the calculated T_{max} of the dense cathode. As a result, the calculated values of T_{max} of the dense sample are lower than those of the porous sample. However, compared to the actually observed values for T_{max} of D-A as 100 ºC and that of D-B as 50 ºC (Figures 3. (a) and 3. (b)), it can be seen that the phenomenon that the calculated T_{max} is higher than actual T_{max} also

appears in dense samples. The activation energies of the porous and dense cathodes were summarized in Tables 5 and 6. Tables 5 and 6 show that generally the dense samples with higher electrical conductivity have lower activation energy than the porous samples. Most of the porous samples have a low activation energy of 0.1 to 0.3 eV, because the mobility of the hole as the main charge carrier in cathodes is similarly high like in dense samples [44].

In summary, the charge carriers in dense and porous cases are holes with high mobilities even at low temperatures. In addition, the phenomenon that the calculated T_{max} was higher than the actual T_{max} occurred in both the dense and the porous cathodes, and it was confirmed that these characteristics did not change even when the microstructure was changed.

3. 3. Microstructural properties

The SEM results of dense and porous samples were summarized respectively in Figures 7 and 8. Fig. 7 shows that D-A and D-B have average particle sizes of 3.15 and 1.21 μm. The particles seem strongly connected to each other in a form of bonding between the particles established during the sintering process. In addition, the porosities of D-A and D-B were 3.8 and 3.2 %, which means that the density is relatively high.

When comparing the porous cathodes in Figure 8 with the D-A and D-B, the microstructures of the H, M, and L samples have an average particle size of 3 μm and an average porosity of 25 %. In the porous cathodes, the particles seem less connected than dense samples, they show the property of inter-particle bonding typical for porous structures with a low density. In addition, the reason that the particles are separated from each other rather than bonding between the particles is that the materials added when making the cathode paste for screen printing were removed during sintering. Although there is no significant difference in particle size between

the porous cathode and the dense cathode, it can be seen that there is a significant difference in density.

Figures 9. (a) and (b) compare the mobility of charge carriers in dense and porous cathodes according to the contact area. The dense cathode has a large contact area between particles or grains, so the amount of charge bottlenecks is minimized. Because of that the pressure applied to the charge carriers decreases, making it easier for them to move, as shown in Fig. 9. (a). However, in the porous cathode as shown in Fig. 9. (b), charge bottlenecks occur because the contact area is small. Due to the charge bottlenecks, the pressure for the charge carrier to move is increased, and the movement is limited [45]. Figures 9. (c) and (d) show the electric path of the charge carriers in the dense and porous cathodes. In the dense cathode, the effective contact area increases and internal blocking decreases, forming a continuous electric path, as shown in Fig. 9. (c). However, in the porous cathode of Fig. 9. (d), internal blocking between particles occurs due to pores. As a result, the electric path becomes discontinuous and the electrical conductivity decreases. In other words, since the effective contact area between the particles of the porous cathode is smaller than that of the dense cathode, the movement of charge carriers is limited, thereby reducing electrical conductivity [46, 47].

In summary, the difference in electrical conductivity between the dense cathode and the porous cathode is caused by density. It can be seen that the dense sample has high electrical conductivity because a continuous electric path is formed between the particles, but the porous sample has low electrical conductivity due to the discontinuous electric path caused by internal blocking.

4. Conclusion

In this study, the electrical conductivity characteristics of SBCO and SBSCO both in their dense and porous microstructures were studied, and several important characteristics were discovered and analyzed.

The dense SBCO and SBSCO showed MIT and metallic behavior in air atmosphere, respectively. However, in porous SBCO and SBSCO, the conductivity behavior changed to semiconductor. In the porous cathode, internal blocking of the charge carrier path occurs between the particles, generating discontinuous electric path. The electrical conductivity of the porous cathode with the upper conductor showed the highest electrical conductivity value under the same experimental conditions compared to the middle and lower conductor samples.

The dense cathodes showed little difference in conductivity under the heating and cooling cycle in air, but the porous cathodes showed relatively higher conductivity during cooling cycle than heating cycle due to thermal activation. The characteristic of the p-type conductor was seen in all dense and porous samples regardless of microstructure. In addition, the dense samples had high conductivity as the applied current decreased, but the porous sample had almost the same conductivity values regardless of the applied current.

Acknowledgments

This work was supported by the National Research Foundation of Korea (NRF) grant funded by the Korean government (MSIT) (No. 2019R1A2C1087534).

Declaration of competing interest

The authors declare that they have no known competing financial interests or personal relationships that could have appeared to influence the work reported in this paper.

References

[1] A.M. Abdalla, S. Hossain, A.T. Azad, P.M.I. Petra, F. Begum, S.G. Eriksson, A.K. Azad. Nanomaterials for solid oxide fuel cells: a review. Renew. Sustain. Energy Rev., 82 (2018) 353-368. http://doi.org/10.1016/j.rser.2017.09.046

[2] K.E.Song, S.H.Woo, S.W.Baek, H. Kang, W.S. Choi, J.Y. Park, J.H. Kim. $SmBa_{1-x}Ca_xCo_2O_{5+d}$ Layered Perovskite Cathodes for Intermediate Temperature-operating Solid Oxide Fuel Cells. Front. Chem. 8 (2021) 1-7. https://doi.org/10.3389/fchem.2020.628813

[3] G. Roh, H. Kim, H. Jeon, K. Yoon. Fuel Consumption and CO_2 Emission Reductions of Ships Powered by a Fuel-Cell-Based Hybrid Power Source. J. Mar. Sci. Eng. 7 (2019). http://doi.org/10.3390/jmse7070230

[4] H. Koide, Y. Someya, Y., T. Yoshida, T. Maruyama. Properties of Ni/YSZ cermet as anode for SOFC. Solid State Ion. 132 (2000) 253-260. http://doi.org/10.1016/S0167-2738(00)00652-4

[5] S.B. Jin, K.S. Kim, S.W. Baek, H.S. Kim, H.I. Kang, W.S. Choi, J.H. Kim. Characterization of layered perovskite nanofibers using electrospinning for cathode materials of low temperature-operating solid oxide fuel cell. New. Renew. Energy. 13 (2017) 50-58. http://doi.org/10.7849/ksnre.2017.6.13.2.050

[6] A. Weber, E.I. Tiffée. Materials and concepts for solid oxide fuel cells (SOFCs) in stationary and mobile applications. J. Power Sources 127 (2004) 273-283. http://doi.org/10.1016/j.jpowsour.2003.09.024

[7] P. Kofstad, R. Bredesen. High temperature corrosion in SOFC environments. Solid State Ionics. 52 (1992) 69-75. http://doi.org/10.1016/0167-2738(92)90092-4

[8] J. Fergus. Effect of cathode and electrolyte transport properties on chromium poisoning in solid oxide fuel cells. Int. J. hydrogen Energy. 32 (2007) 3664-3671. http://doi.org/10.1016/j.ijhydene.2006.08.005

[9] N. Schrödl, E. Bucher, A. Egger, P. Kreiml, C. Teichert, T. Hoeschen, W. Sitte. Long-term stability of the IT-SOFC cathode materials La0.6Sr0.4CoO3-d and La2NiO4+d against combined chromium and silicon poisoning. Solid State Ionics. 276 (2015) 62-71. https://doi.org/10.1016/j.ssi.2015.03.035

[10] S.W. Song, W.S. Choi, H. Kang, S.W. Baek, A.K. Azad, J.Y. Park, J.H. Kim. Synthesis and electrochemical properties of layered perovskite substituted with heterogeneous lanthanides for intermediate temperature-operating solid oxide fuel cell. Int. J. hydrogen Energy. 43 (2018) 11378-11385. https://doi.org/10.1016/j.ijhydene.2018.04.011

[11] J. Molenda, K. Swierczek, W. Zajac. Functional materials for the IT-SOFC. J. Power Sources. 173 (2007) 657-670. https://doi.org/10.1016/j.jpowsour.2007.05.085

[12] E. Fabbri, L. Bi, D. Pergolesi, E. Traversa. Towards the next generation of solid oxide fuel cells operating below 600 ºC with chemically stable proton-conducting electrolytes. Adv. Mater. 24 (2012) 195-208. https://doi.org/10.1002/adma.201103102

[13] S.W. Baek, A.K. Azad, J.T.S. Irvine, W.S. Choi, H.I. Kang, J.H. Kim, Electrochemical properties of composite cathodes using Sm doped layered perovskite for intermediate temperature-operating solid oxide fuel cell. Appl. Surf. Sci. 432 (2018) 272-277. https://doi.org/10.1016/j.apsusc.2017.02.211.

[14] J.H. Kim, Y.M Kim, P.A. Connor, J.T.S. Irvine, J.M. Bae, W. Zhou. Structural, thermal and electrochemical properties of layered perovskite SmBaCo2O5+d, a potential cathode material for intermediate-temperature solid oxide fuel cells. J. Power Sources. 194 (2009) 704–

711. https://doi.org/10.1016/j.jpowsour.2009.06.024.

[15] Z. Gao, L.V. Mogni, E.C. Miller, J.G. Railsback, S.A. Barnett. A perspective on low-temperature solid oxide fuel cells. Energy Environ. Sci. 9 (2016) 1602-1644. https://doi.org/10.1039/C5EE03858H

[16] Y. Tao, J. Shao, J. Wang, W.G. Wang. Synthesis and properties of La0.6Sr0.4CoO3-δ nanopowder. J. Power Sources, 185 (2008) 609-614. http://doi.org/10.1016/j.jpowsour.2008.09.021

[17] S. Pang, X. Jiang, X. Li, Z. Su, H. Xu, Q. Xu, C. Chen. Characterization of cation-ordered perovskite oxide LaBaCo2O5+δ as cathode of intermediate-temperature solid oxide fuel cells. Int. J. Hydrogen Energy, 37 (2012) 6836-6843. http://doi.org/10.1016/j.ijhydene.2012.01.056

[18] P. Zhang, G. Guan, D.S. Khaerudini, X. Hao, C. Xue, M. Han, Y. Kasai, A. Abudula. B-site Mo-doped perovskite Pr0.4Sr0.6(Co0.2Fe0.8)1-xMoxO3-σ (x=0, 0.05, 0.1 and 0.2) as electrode for symmetrical solid oxide fuel cell. J. Power Sources, 276 (2015) 347-356. http://doi.org/10.1016/j.jpowsour.2014.11.141

[19] Q. Zhou, Y. Zhang, Y. Shen, T. He. Layered perovskite GdBaCuCoO5+δ cathode material for intermediate-temperature solid oxide fuel cells. J. Electrochem. Soc. 157 (2010) B628-B632. http://doi.org/10.1149/1.3321725

[20] J. Piao, K. Sun, N. Zhang, X. Chen, S. Xu, D. Zhou. Preparation and characterization of Pr1-xSrxFeO3 cathode material for intermediate temperature solid oxide fuel cells. J. Power Sources, 172 (2007) 633-640. http://doi.org/10.1016/j.jpowsour.2007.05.023

[21] J.W. Yin, Y.M. Yin, J. Lu, C. Zhang, N.Q. Minh, Z.F. Ma. Structure and properties of novel cobalt-free oxides NdxSr1-xFe0.8Cu0.2O3-δ (0.3≤x≤0.7) as cathodes of intermediate temperature solid oxide fuel cells. J. Phys. Chem. C, 118 (2014) 13357-13368.

http://doi.org/10.1021/jp500371w

[22] D. Gostovic, J. R. Smith, D. P. Kundinger, K. S. Jones, E. D. Wachsman. Three-Dimensional Reconstruction of Porous LSCF Cathodes. Electrochemical and Solid-State Letters, 10 (2007) B214-B217. http://doi.org/10.1149/1.2794672

[23] J. R. Wilson, W. Kobsiriphat, R. Mendoza, H. Y. Chen, J. M. Hiller, D. J. Miller, K. Thornton, P. W. Voorhees, S. B. Adler, and S. A. Barnett. Three-dimensional reconstruction of a solid-oxide fuel-cell anode. Nat. Mater. 5 (2006) 541-544. http://doi.org/10.1038/nmat1668

[24] M.A.Yatoo, S.J. Skinner. Ruddlesden-Popper phase materials for solid oxide fuel cell cathodes: A short review. Mater. Today Proc. (2022) 10-17. https://doi.org/10.1016/j.matpr.2021.12.537

[25] J.T.S. Irvine, D. Neagu, M.C. Verbraeken, C. Chatzichristodoulou, C. Graves, M.B. Mogensen. Evolution of the electrochemical interface in high-temperature fuel cells and electrolysers. Nat. Energy. 1 (2016) 15014. https://doi.org/10.1038/nenergy.2015.14

[26] A. Grimaud, F. Mauvy, J. Marc Bassat, S. Fourcade, M. Marrony, J. Claude Grenier. Hydration and transport properties of the $Pr_{2-x}Sr_xNiO_{4+\delta}$ compounds as H^+-SOFC cathodes. J. Mater. Chem., 22 (2012) 16017-16025. https://doi.org/10.1039/C2JM31812A

[27] M. Marinsek. Electrical conductivity of sintered LSM ceramics. Mater. Technol. 43 (2009) 79-84. http://mit.imt.si/Revija/izvodi/mit092/marinsek.pdf

[28] O.O. Agbede, K. Hellgardta, G.H. Kelsall. Electrical conductivities and microstructures of LSM, LSM-YSZ and LSM-YSZ/LSM cathodes fabricated on YSZ electrolyte hollow fibres by dip-coating. 16 (2020) 100252. https://doi.org/10.1016/j.mtchem.2020.100252

[29] K.S. Baek, S.W. Baek, H. Kang. W.S. Choi, J.Y. Park, S. Saxin, S.K. Lee, J.H. Kim.

Electrical conductivity characteristics of Sr substituted layered perovskite cathode ($SmBa_{0.5}Sr_{0.5}Co_2O_{5+d}$) for intermediate temperature-operating solid oxide fuel cell. Ceram. Int. 17 (2022). https://doi.org/10.1016/j.ceramint.2022.02.114

[30] K.E. Song, J.W. Lee, Y.R. Lim, S.W. Baek, T.H. Shin, S.K. Lee, H. Schlegl, J.H. Kim. Influence of microstructure and applied current on the electrical conductivity of $SmBaCo_2O_{5+d}$ cathode in solid oxide fuel cell. Int. J. Hydrogen Energy. (2022) https://doi.org/10.1016/j.ijhydene.2022.03.056

[31] J.H. Kim, M. Cassidy, J.T.S. Irvine, J.M. Bea. Advanced Electrochemical Properties of LnBa0.5Sr0.5Co2O5+d (Ln = Pr, Sm, and Gd) as Cathode Materials for IT-SOFC. J. Electrochem. Soc. 156 (2009) B682–B689. https://doi.org/10.1149/1.3110989

[32] J.H. Kim, M. Cassidy, J.T.S. Irvine, J.M. Bea. Electrochemical investigation of composite cathodes with SmBa0.5Sr0.5Co2O5+d cathodes for intermediate temperature-operating solid oxide fuel cell. Chem. Mater. 22 (2010) 883–892. https://doi.org/10.1021/cm901720w

[33] J.T.S. Irvine, J.M. Bea, J.Y. Park, W.S. Choi, J.H. Kim. Electrochemical properties and durability of in-situ composite cathodes with SmBa0.5Sr0.5Co2O5+δ for metal supported solid oxide fuel cells. Int. J. Hydrogen Energy. 42 (2017) 1212–1220. https://doi.org/10.1016/j.ijhydene.2016.10.158

[34] J.H. Kim, Comparison of Electrical Conductivities in Complex Perovskites and Layered Perovskite for Cathode Materials of Intermediate Temperature-operating Solid Oxide Fuel Cell. J. Korean Ceram. Soc. 51 (2014) 295-299. https://doi.org/10.4191/kcers.2014.51.4.295.

[35] D. Chaudhuri, P.W. Menezes, D.D. Sarma. Remarkable thermal stability of BF3-doped polyaniline. Appl. Phys. Lett. 83 (2003) 2348-2350. https://doi.org/10.1063/1.1613797

[36] S. Kim, Y.L. Yang, R. Christoffersen, A.J. Jacobson. Oxygen permeation, electrical

conductivity and stability of the perovskite oxide La0.2Sr0.8Cu0.4Co0.6O3-x. Solid State Ionics 104 (1997) 57-65. https://doi.org/10.1016/S0167-2738(97)00427-X

[37] V. Cascos, R. Martı´nez-Coronado, J.A. Alonso, M.T. Fernandez-Dı´az. Structural and electrical characterization of the Co-doped Ca2Fe2O5 brownmillerite: Evaluation as SOFC - cathode materials. Int. J. hydrogen energy. 40 (2015) 5456-5468. https://doi.org/10.1016/j.ijhydene.2015.01.067

[38] A. Aguadero, D. Pérez-Coll, J. A. Alonso, S. J. Skinner, J. Kilner. A New Family of Mo-Doped SrCoO3−δ Perovskites for Application in Reversible Solid State Electrochemical Cells. Chem. Mater. 24 (2012) 2655-2663. http://doi.org/10.1021/cm300255r

[39] J.H. Chan, J.A. Bock, H. Guo, S. Trolier-Mckinstry, C.A. Randall. High-temperature thermoelectric characterization of filled strontium barium niobates: power factors and carrier concentrations. J. Mater. Res. 32 (2017) 1160-1167. https://doi.org/10.1557/jmr.2017.18

[40] J.H. Park, D. Kim, K.J. Kim, K.T. Lee. A brief review of the bilayer electrolyte strategy to achieve high performance solid oxide fuel cells. Ceramist 23 (2020) 184-199. https://doi.org/10.31613/ceramist.2020.23.2.02

[41] J.S. Park, H.G. Kim. Electrical Conductivity and Defect Models of MgO-Doped Cr2O3. J. Am. Ceram. Soc. 71(3) (1988) 173-176. https://doi.org/10.1111/j.1151-2916.1988.tb05024.x

[42] H.S. Lee, S.M. Chung, S.Y. Yang, J.H. Seo. Radio-Frequency Thermal Plasma Synthesis of LSCF Nano-Powders for Cathode Applications in IT-SOFC. Korean hydrogen and New Energy 32 (2021) 100-108. https://doi.org/10.7316/KHNES.2021.32.2.100

[43] L.W. Tai, M.M. Nasrallah, H.U. Anderson, D.M. Sparlin, S.R. Sehlin. Structure and electrical properties of La1−xSrxCo1−yFeyO3. Part 2. The system La1-xSrxCo0.2Fe0.8O3. Solid State Ionics 76 (1995) 273-283. http://doi.org/10.1016/0167-2738(94)00245-n

[44] A.A. Samat, A.A. Jais, M.R. Somalu, N. Osman, A. Muchtar, K.L. Lim, Electrical and electrochemical characteristics of $La_{0.6}Sr_{0.4}CoO_{3-\delta}$ cathode materials synthesized by a modified citrate-EDTA sol-gel method assisted with activated carbon for proton-conducting solid oxide fuel cell application, J. Sol-Gel. Sci. Tech. 86 (2018) 617-630. https://doi.org/10.1007/s10971-018-4675-1

[45] K.Y. Park, J.M. Lim, N.S. Luu, J.R. Downing, S.G. Wallace, L.E. Chaney, H. Yoo, W.J. Hyun, H.U. Kim, M.C. Hersam. Concurrently Approaching Volumetric and Specific Capacity Limits of Lithium Battery Cathodes via Conformal Pickering Emulsion Graphene Coatings. Adv. Energy Mate. 10 (2020) 1-11. https://doi.org/10.1002/aenm.202001216

[46] S. Paydar, M.H. Shariat, S. Javadpour. Investigation on electrical conductivity of LSM/YSZ8, LSM/$Ce_{0.84}Y_{0.16}O_{0.96}$ and LSM/$Ce_{0.42}Zr_{0.42}Y_{0.16}O_{0.96}$ composite cathodes of SOFCs. Int. J. Hydrogen Energy. 41 (2016) 23145–23155. https://doi.org/10.1016/j.ijhydene.2016.10.092

[47] H.E. Khal, A. Cordier, N. Batis, E. Siebert, S. Georges, M.C. Steil. Effect of porosity on the electrical conductivity of LAMOX materials. Solid State Ionics. 304 (2017) 75-84. http://doi.org/10.1016/j.ssi.2017.03.028

Figure captions

Fig. 1. Schematic diagrams of (a) upper conductor, (b) middle conductor and (c) lower conductor samples

Fig. 2. X-ray diffraction (XRD) results of $SmBaCo_2O_{5+d}$ (A) and $SmBa_{0.5}Sr_{0.5}Co_2O_{5+d}$ (B) oxide systems.

Fig. 3. Electrical conductivity results of (a) D-A and H-AG and (b) D-B and H-BG. In this figure, heating cycle indicates that measurements were carried out while raising the temperature and cooling cycle indicates that measurements were carried out while lowering the temperature starting from a temperature maximum

Fig. 4. The electrical conductivities of porous microstructural cathodes; under air atmosphere (a) at heating cycle and (b) cooling cycle, under nitrogen atmosphere (c) at heating cycle and (d) cooling cycle

Fig. 5. The electrical conductivities of H-BG porous microstructural cathodes with upper conductor

Fig. 6. The electrical conductivities of H-BG sample according to applied currents; under air atmosphere at (a) heating cycle and (b) cooling cycle and under nitrogen atmosphere at (c) heating cycle and (d) cooling cycle

Fig. 7. Surface microstructural properties of D-A and D-B

Fig. 8. Surface microstructural properties of (a) upper conductor, (b) middle conductor and (c) lower conductor samples

Fig. 9. Comparison of small area contact and large area contact between particles in cathodes; Charge transport pathways arising from (a) large-area contacts of dense cathodes and (b) small-

area contacts of porous cathodes and conceptual depictions of an electric path (red lines) of (c) dense cathodes and (d) porous cathodes

Table captions

Table 1. Electrical conductivities of cathodes in literature

Table 2. Abbreviation of dense microstructure samples

Table 3. Abbreviation of porous microstructural samples

Table 4. Calculated T_{max} from activation energies (listed in Table 4) of porous microstructural samples by applying current of 0.05 A

Table 5. Calculated T_{max} from activation energies of dense microstructural samples

Table 6. Calculated activation energies for the electrical conductivities at 400 ~ 650 ºC of all samples

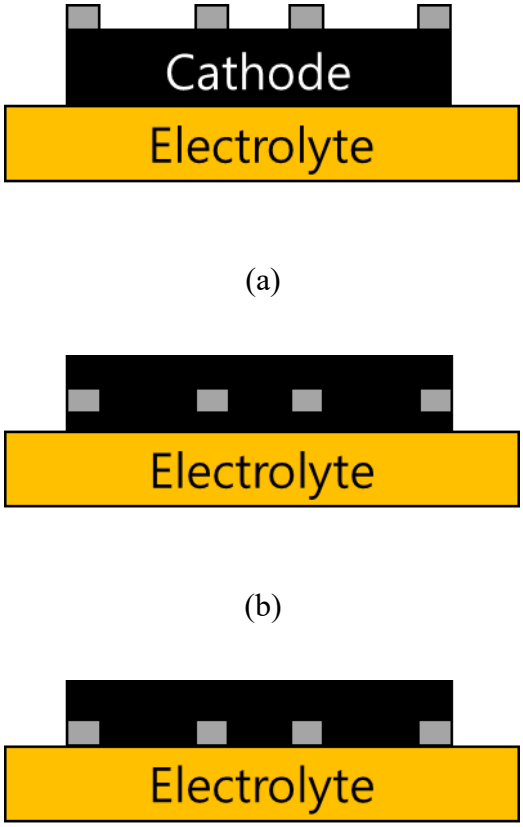

Fig. 1. Schematic diagrams of (a) upper conductor, (b) middle conductor and (c) lower conductor samples

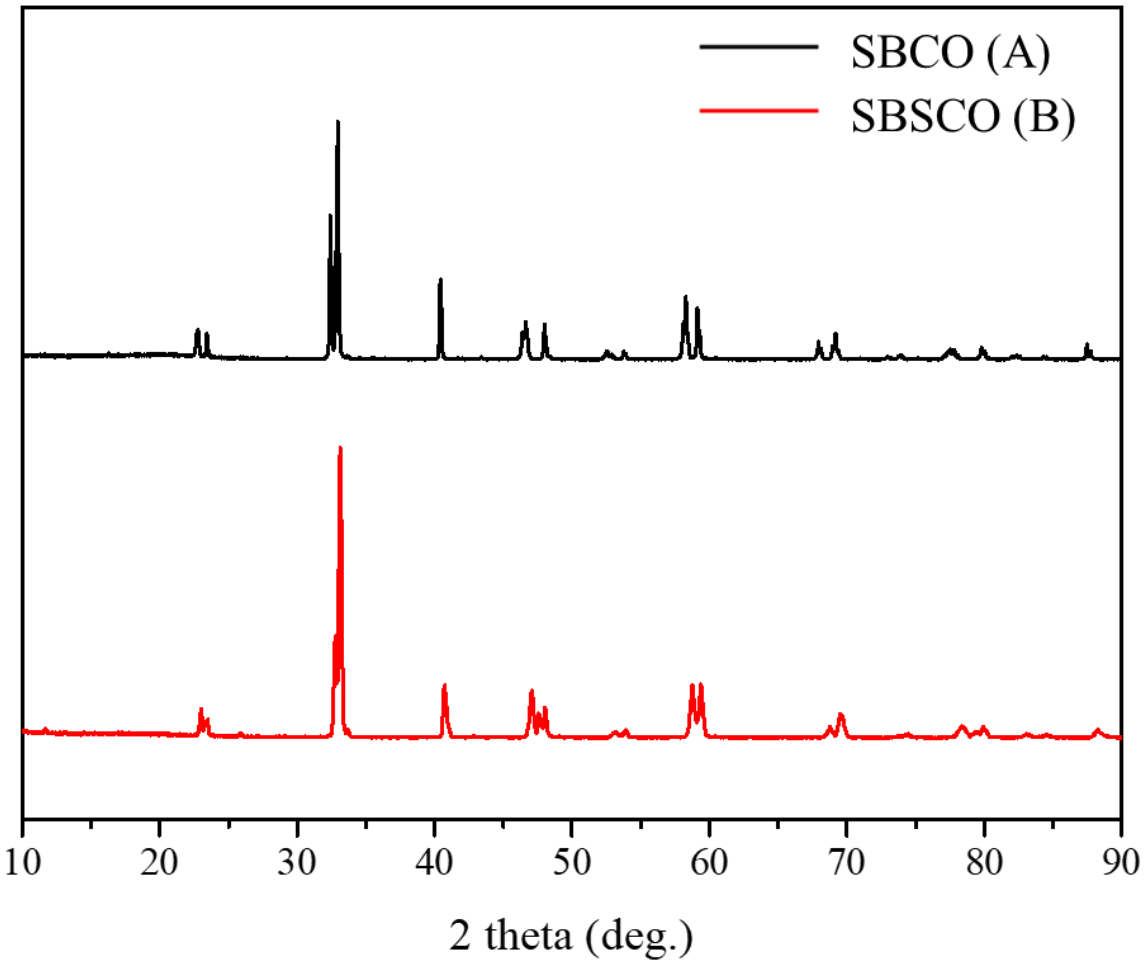

Fig. 2. X-ray diffraction (XRD) results of $SmBaCo_2O_{5+d}$ (A) and $SmBa_{0.5}Sr_{0.5}Co_2O_{5+d}$ (B) oxide systems.

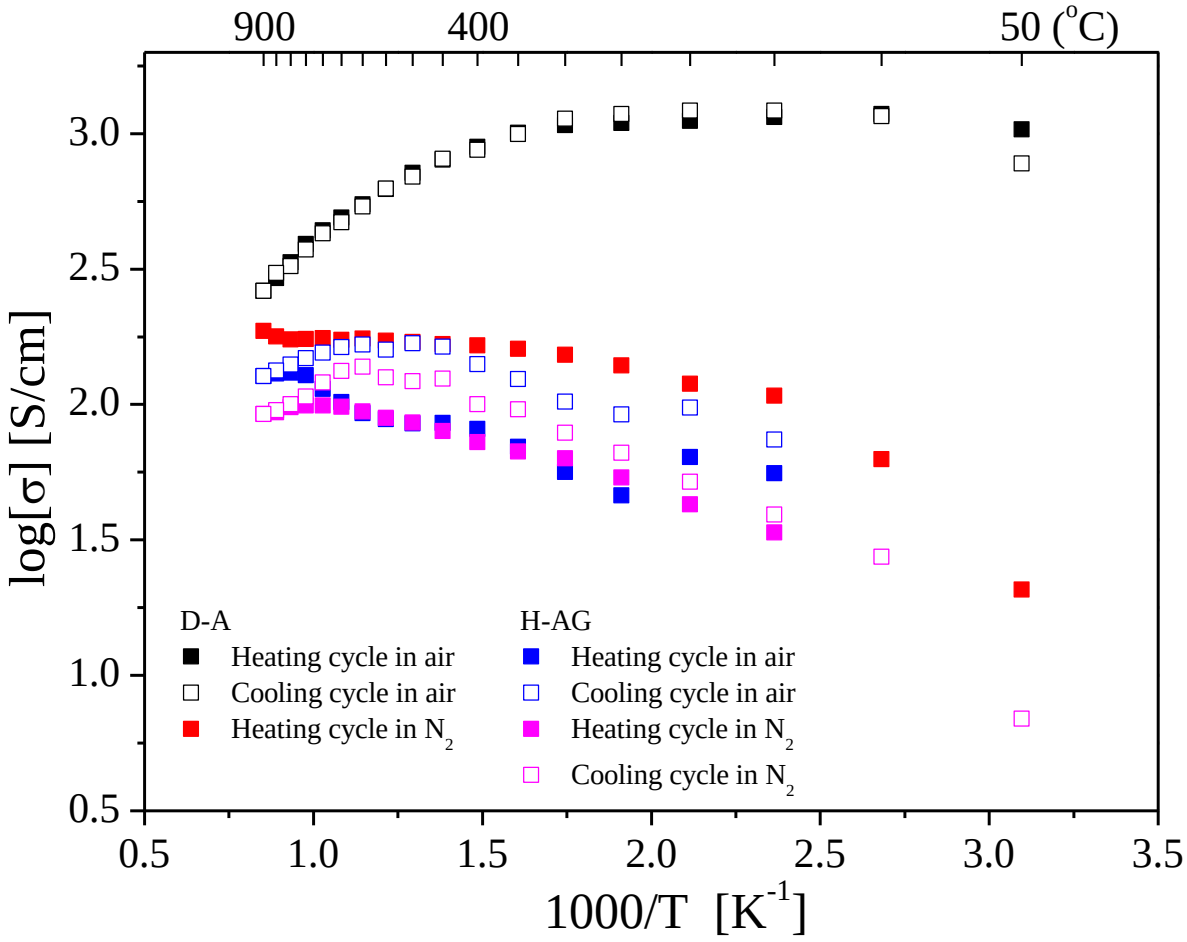
900
400
50 (°C)
3.0
2.5
2.0
1.5
1.0
0.5
log[σ] [S/cm]
D-A
Heating cycle in air
Cooling cycle in air
Heating cycle in N2
H-AG
Heating cycle in air
Cooling cycle in air
Heating cycle in N2
Cooling cycle in N2
0.5
1.0
1.5
2.0
2.5
3.0
3.5
1000/T [K-1]

(a)

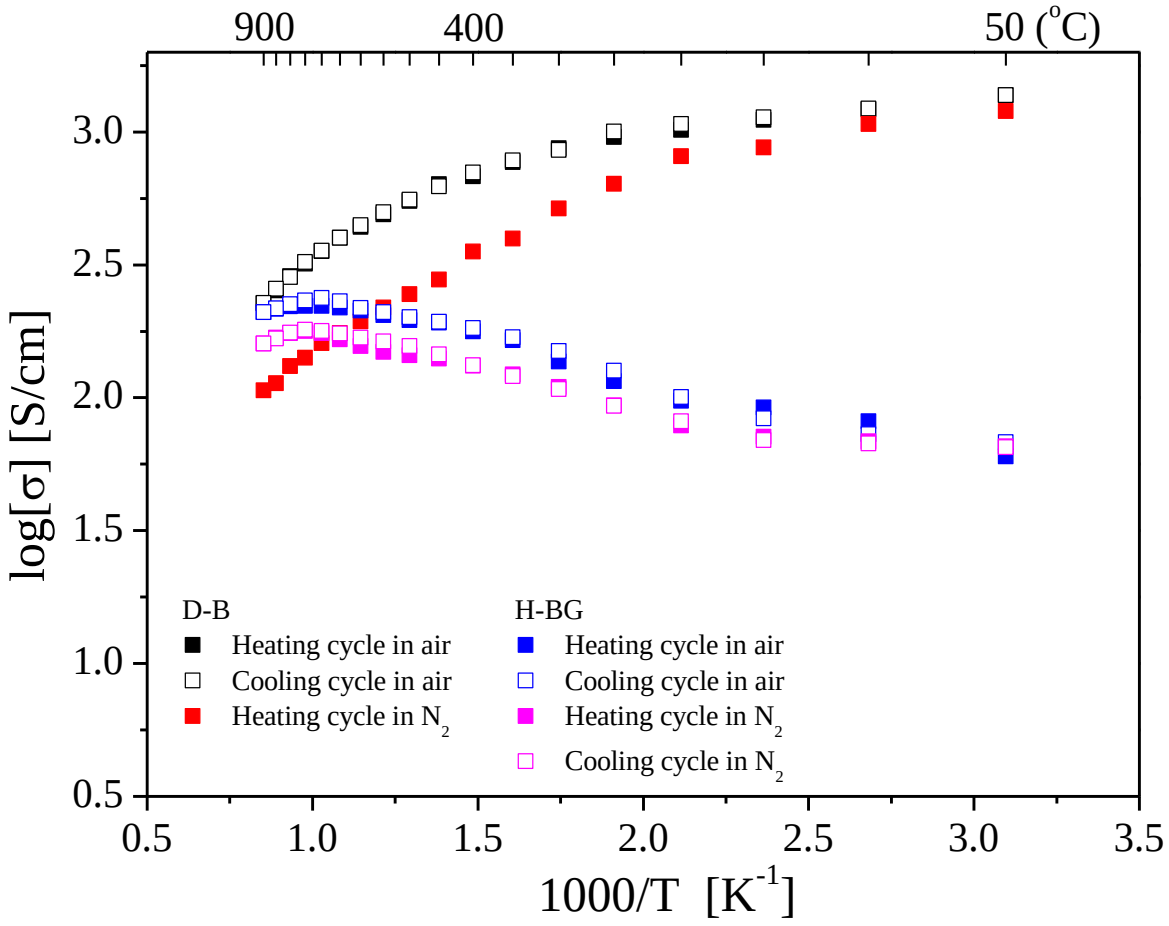

(b)

Fig. 3. Electrical conductivity results of (a) D-A and H-AG and (b) D-B and H-BG. In this figure, heating cycle indicates that measurements were carried out while raising the temperature and cooling cycle indicates that measurements were carried out while lowering the temperature starting from a temperature maximum.

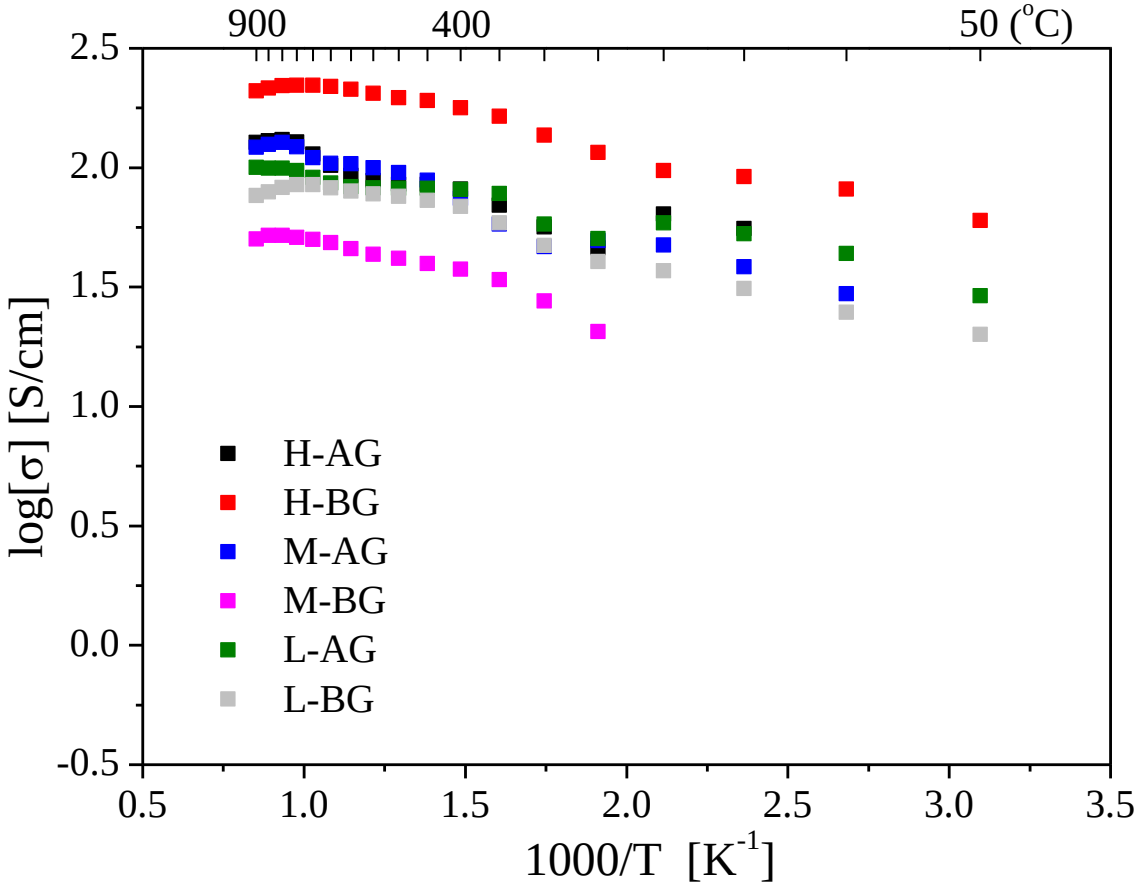
900
400
50 (°C)
2.5
2.0
1.5
1.0
0.5
0.0
-0.5
log[σ] [S/cm]
H-AG
H-BG
M-AG
M-BG
L-AG
L-BG
0.5
1.0
1.5
2.0
2.5
3.0
3.5
1000/T [K-1]

(a)

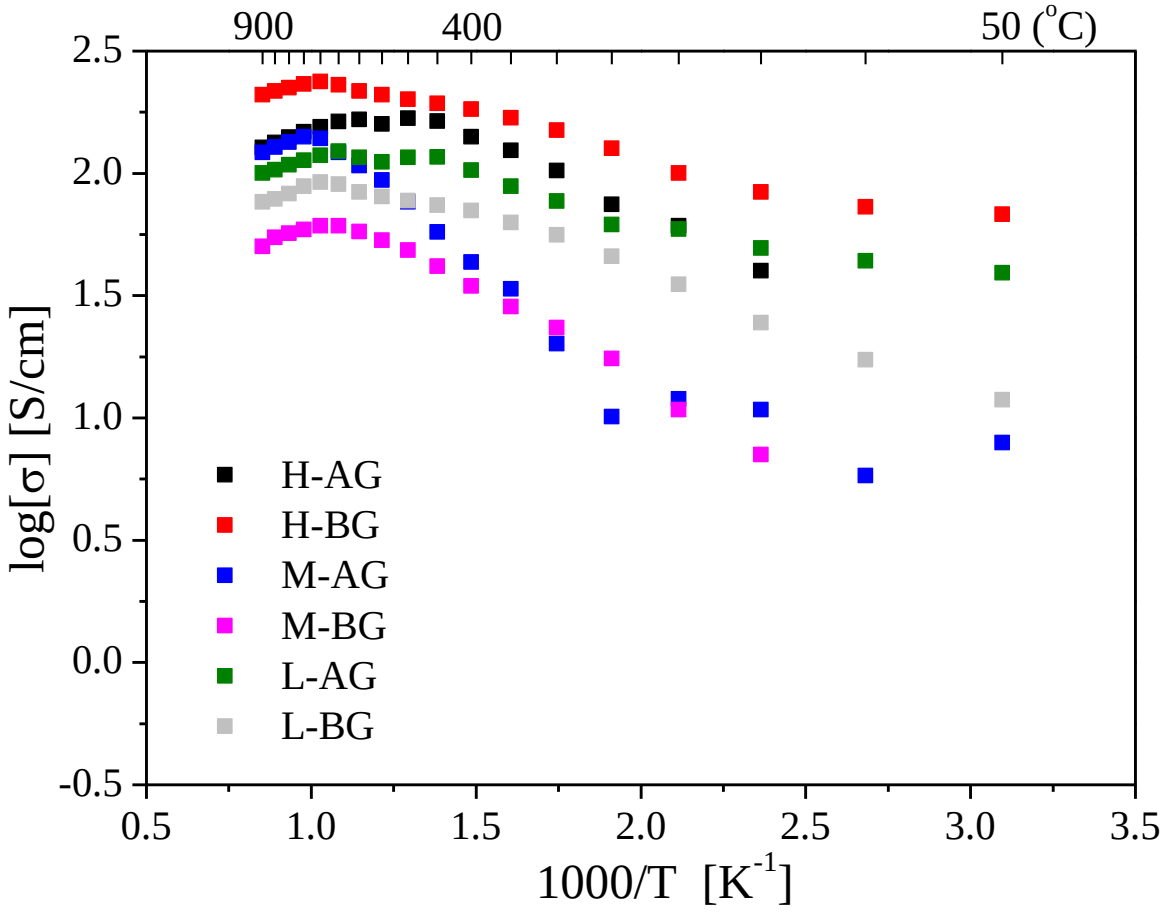
900
400
50 (°C)
2.5
2.0
1.5
1.0
0.5
0.0
-0.5
log[σ] [S/cm]
H-AG
H-BG
M-AG
M-BG
L-AG
L-BG
0.5
1.0
1.5
2.0
2.5
3.0
3.5
1000/T [K-1]

(b)

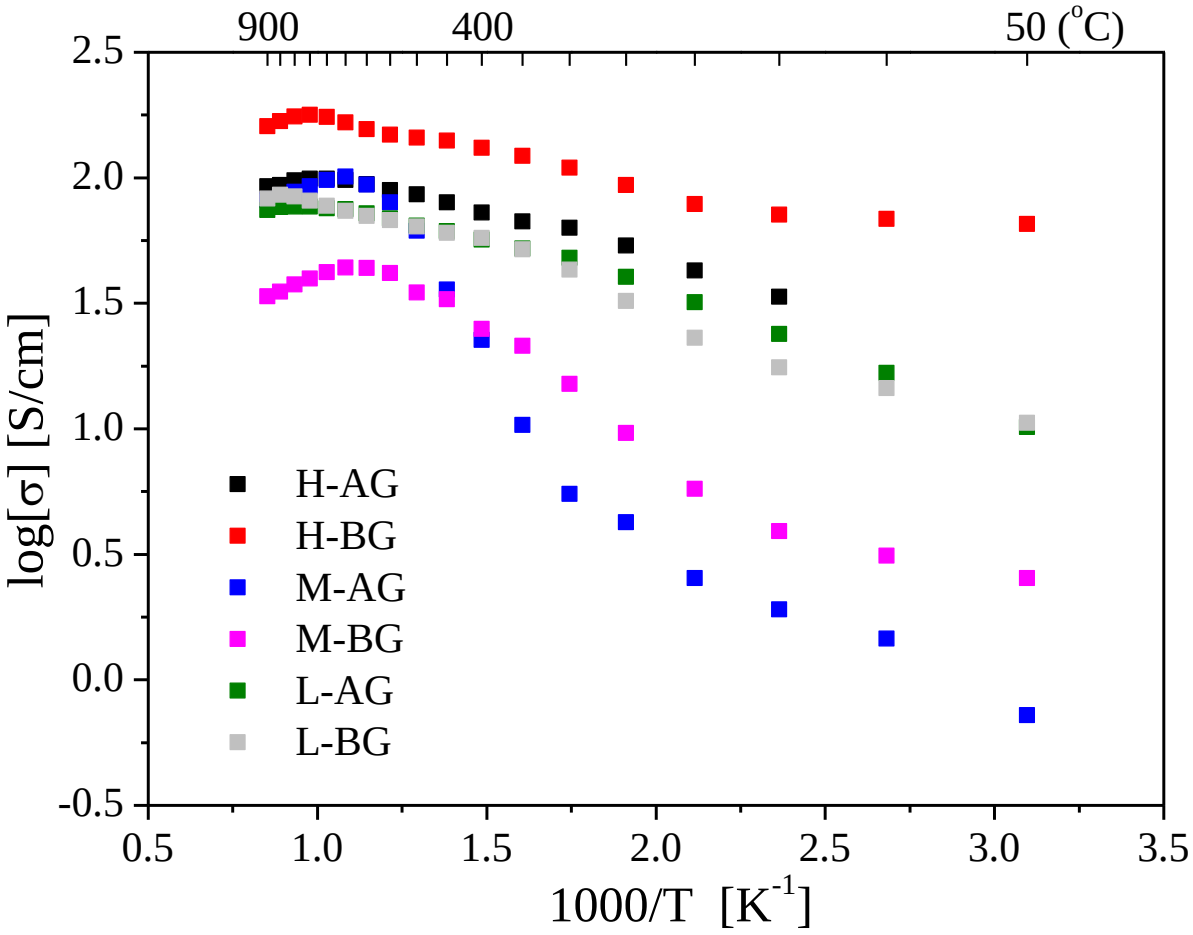
900
400
50 (°C)
2.5
2.0
1.5
1.0
0.5
0.0
-0.5
log[σ] [S/cm]
H-AG
H-BG
M-AG
M-BG
L-AG
L-BG
0.5
1.0
1.5
2.0
2.5
3.0
3.5
1000/T [K-1]

(c)

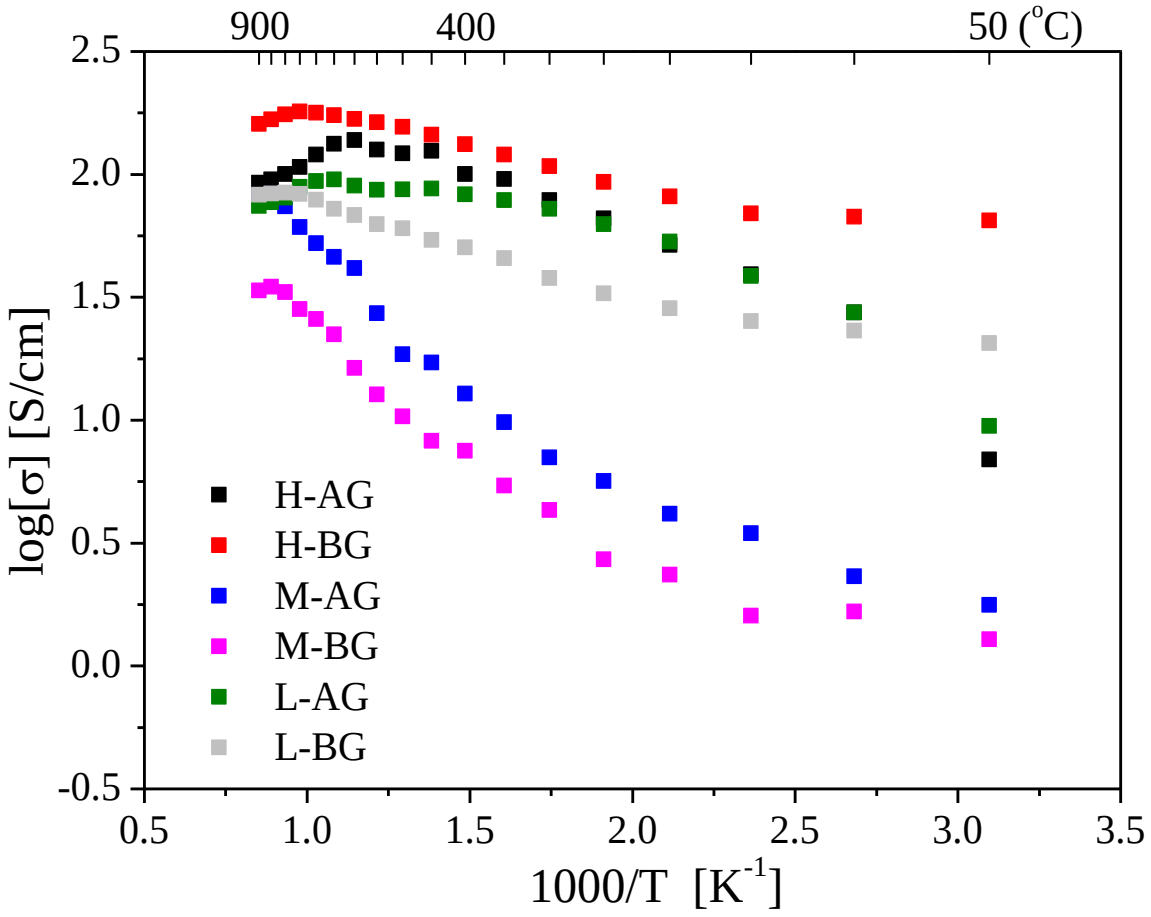

(d)

Fig. 4. The electrical conductivities of porous microstructural cathodes; under air atmosphere (a) at heating cycle and (b) cooling cycle, under nitrogen atmosphere (c) at heating cycle and (d) cooling cycle

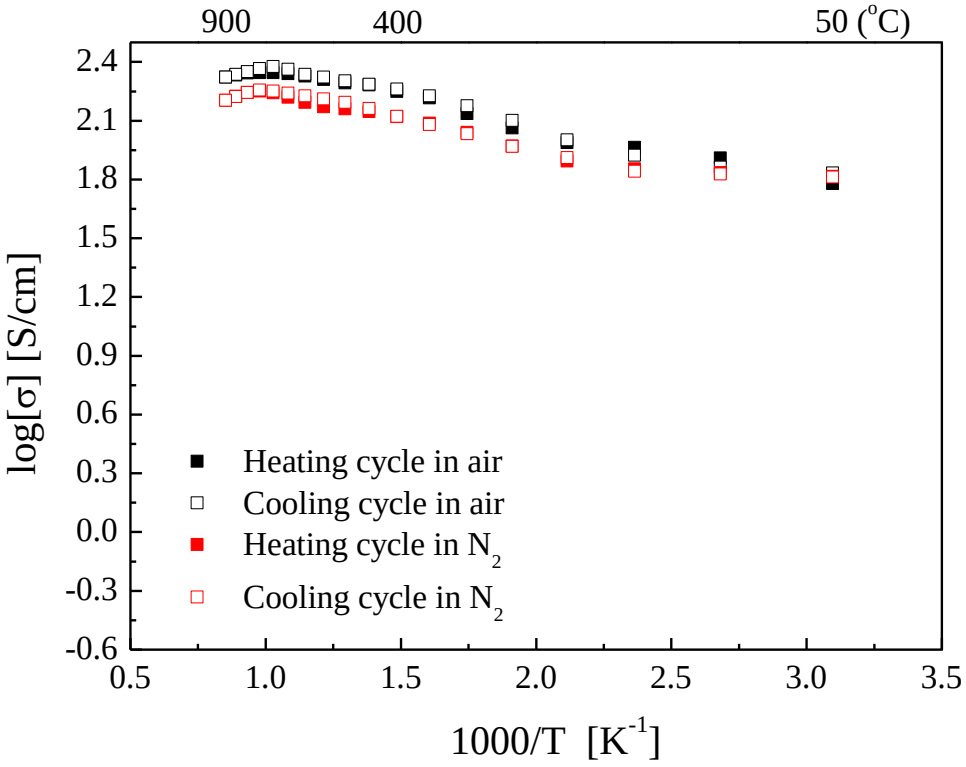

Fig. 5. The electrical conductivities of H-BG porous microstructural cathodes with upper conductor

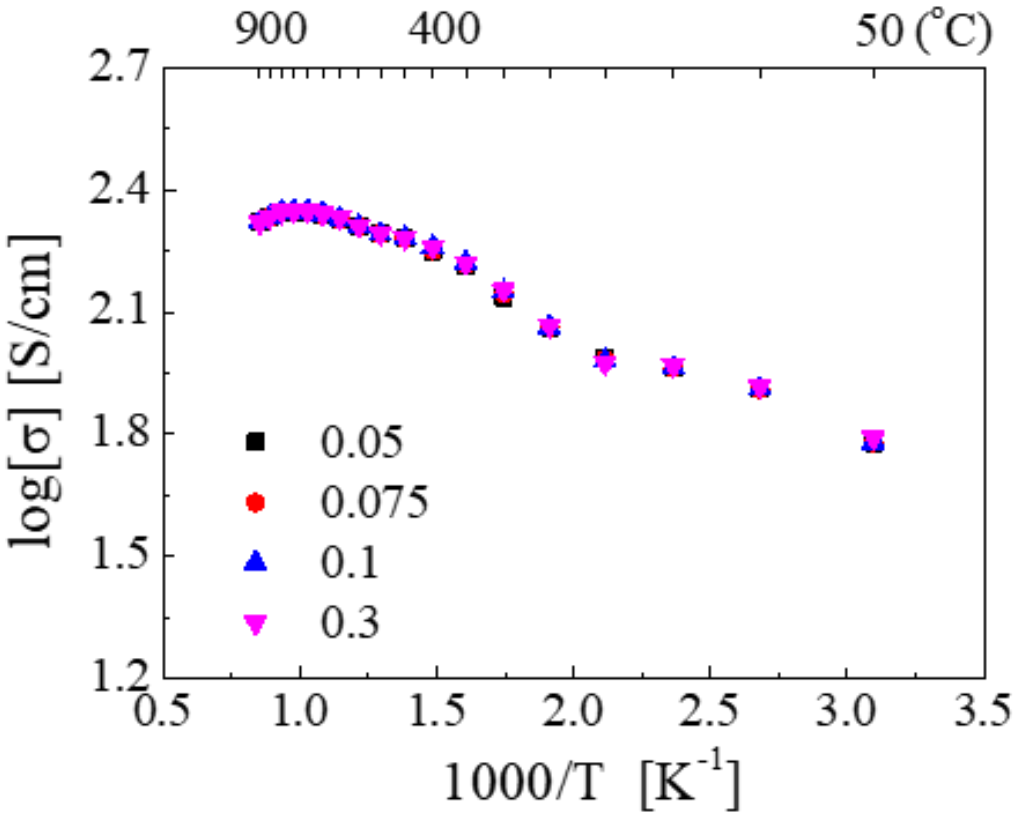
900
400
50 (°C)
2.7
2.4
2.1
1.8
1.5
1.2
log[σ] [S/cm]
0.05
0.075
0.1
0.3
0.5
1.0
1.5
2.0
2.5
3.0
3.5
1000/T [K-1]

(a)

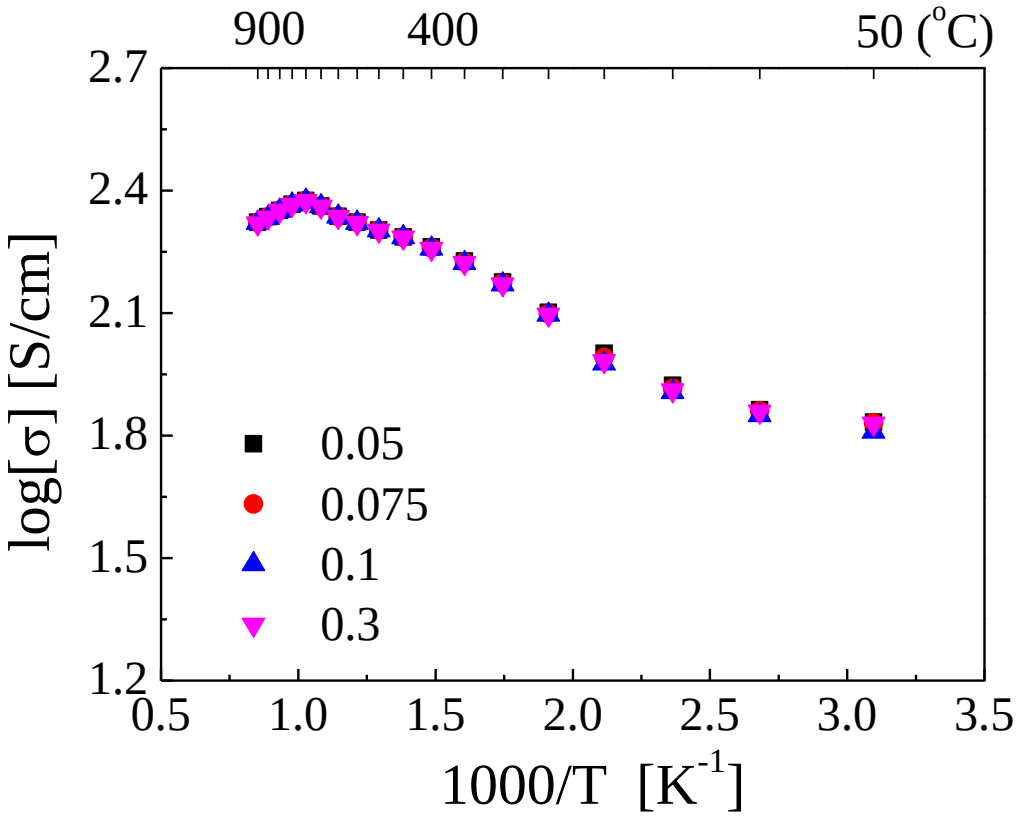
900
400
50 (°C)
2.7
2.4
2.1
1.8
1.5
1.2
log[σ] [S/cm]
0.05
0.075
0.1
0.3
0.5
1.0
1.5
2.0
2.5
3.0
3.5
1000/T [K-1]

(b)

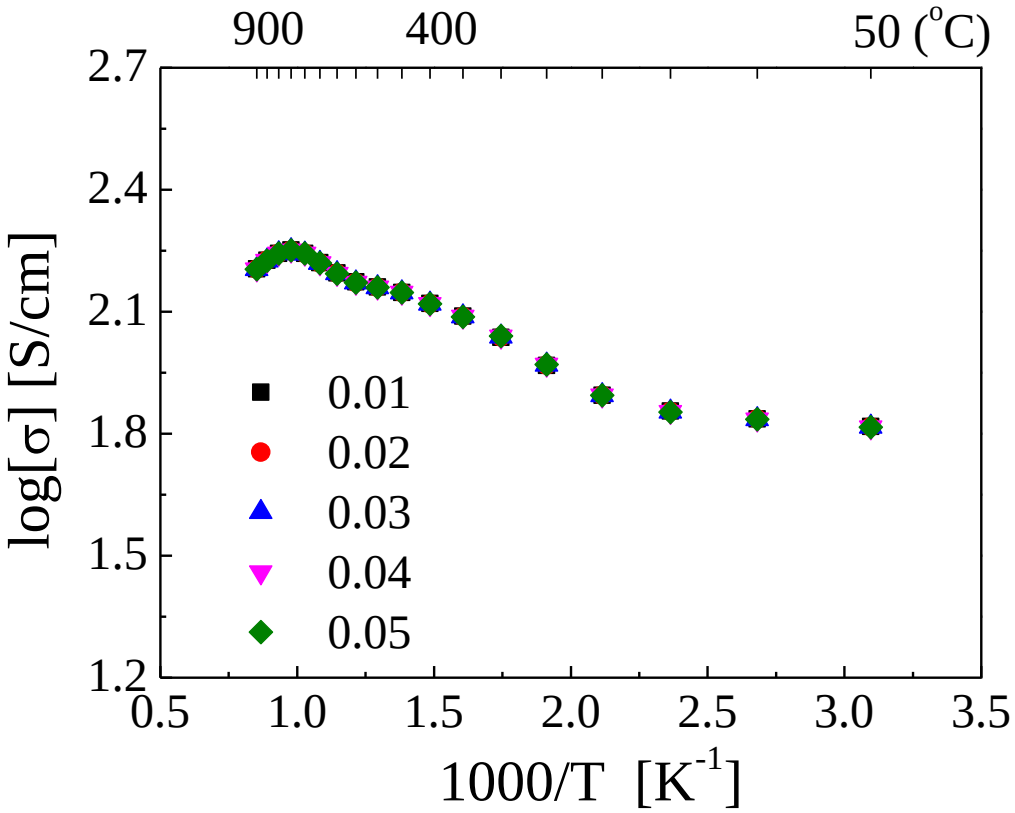
900
400
50 (°C)
2.7
2.4
2.1
1.8
1.5
1.2
log[σ] [S/cm]
0.01
0.02
0.03
0.04
0.05
0.5
1.0
1.5
2.0
2.5
3.0
3.5
1000/T [K-1]

(c)

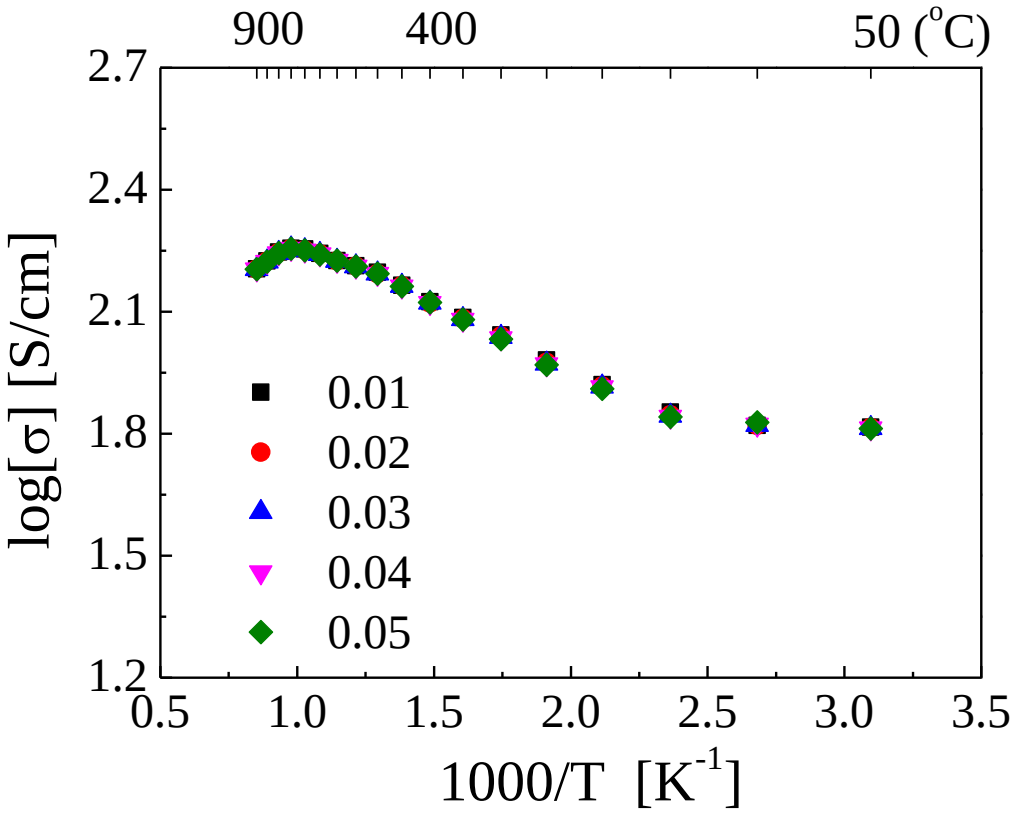

(d)

Fig. 6. The electrical conductivities of H-BG sample according to applied currents; under air atmosphere at (a) heating cycle and (b) cooling cycle and under nitrogen atmosphere at (c) heating cycle and (d) cooling cycle

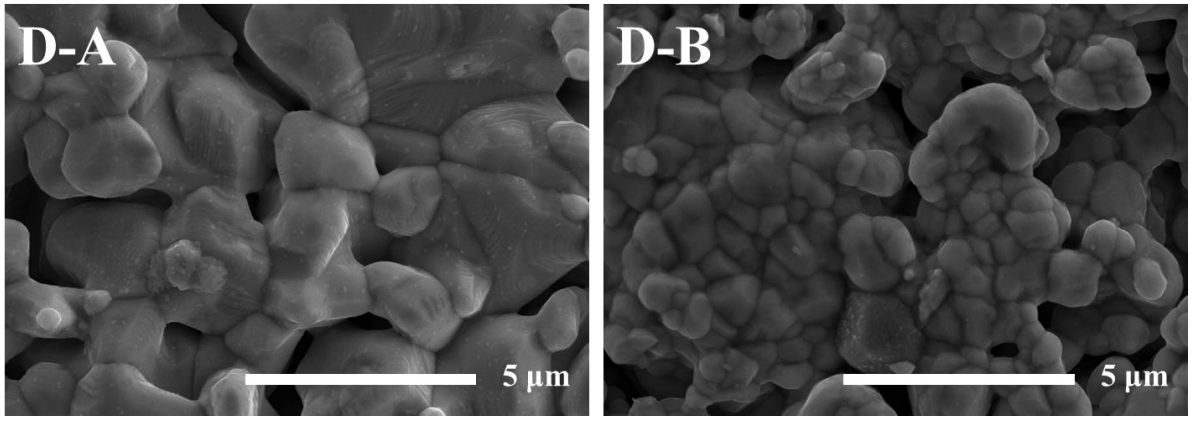

Fig. 7. Surface microstructural properties of D-A and D-B

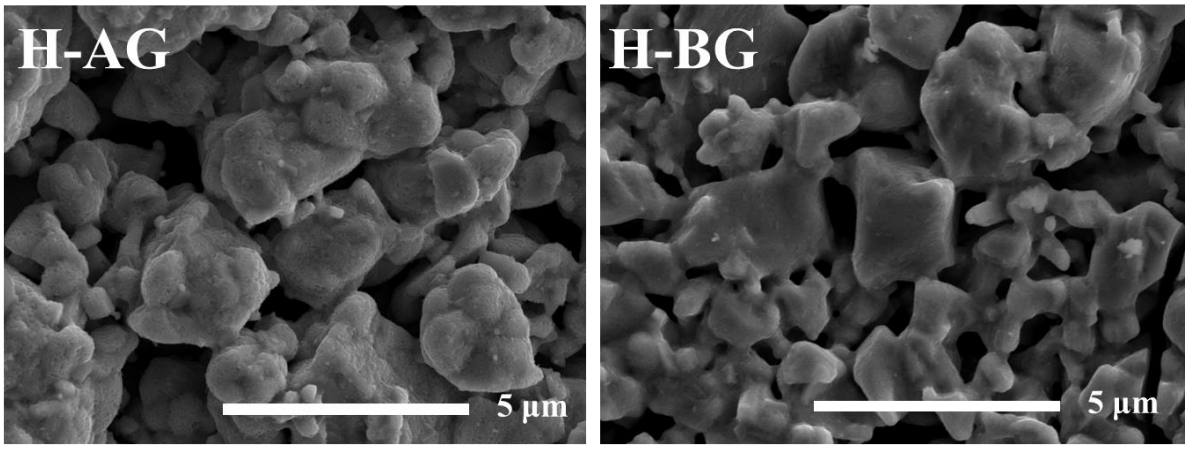

(a)

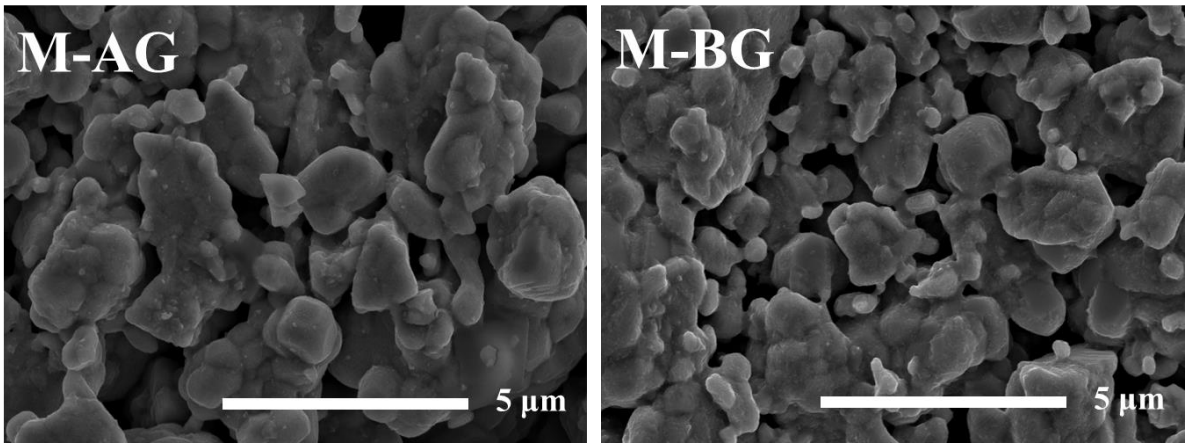

(b)

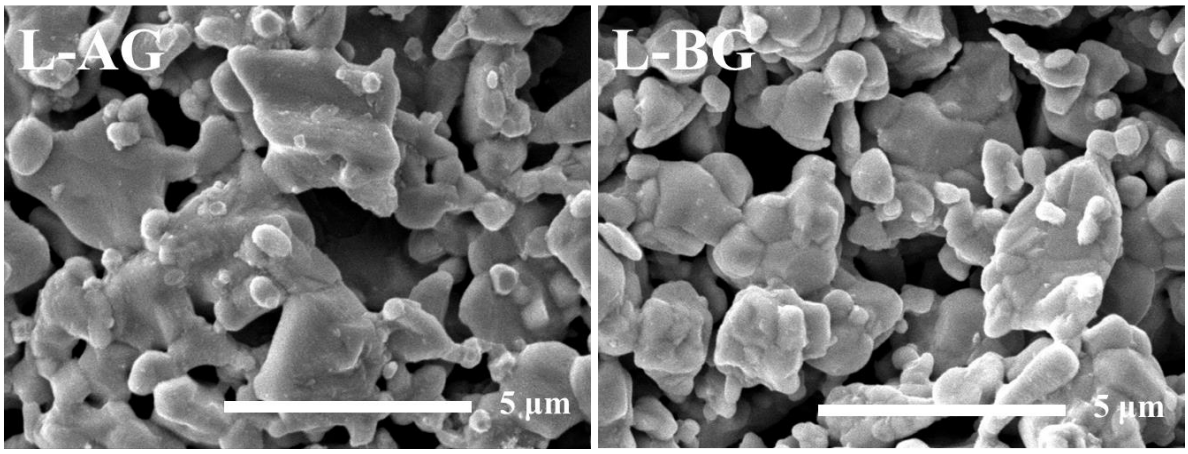

(c)

Fig. 8. Surface microstructural properties of (a) upper conductor, (b) middle conductor and (c) lower conductor samples

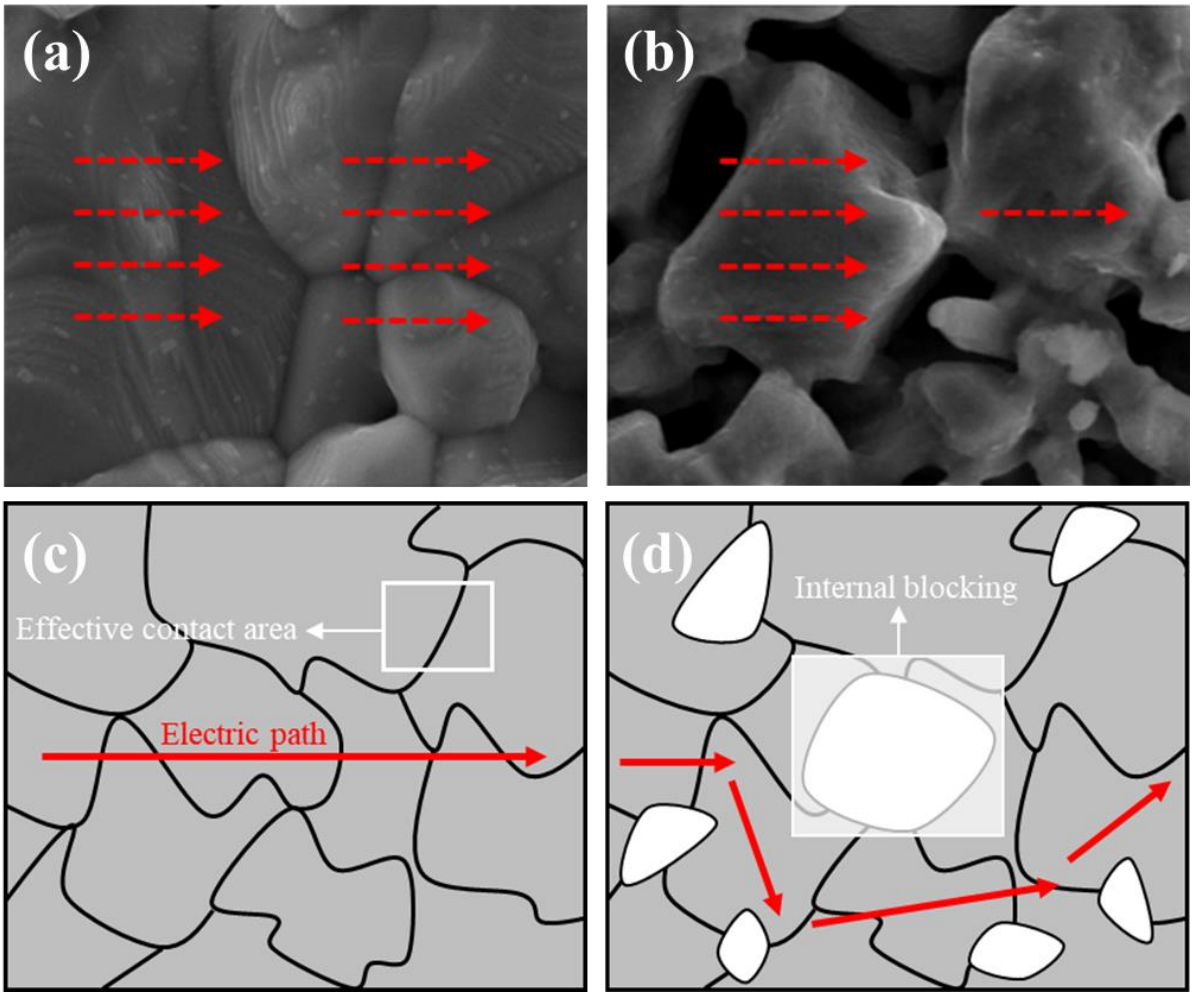

Fig. 9. Comparison of small contact area and large contact area between particles in cathodes; Charge transport pathways arising from (a) large-area contacts of dense cathodes and (b) small-area contacts of porous cathodes and conceptual depictions of an electric path (red lines) of (c) dense cathodes and (d) porous cathodes

Table 1. Electrrical conductivities of cathodes in literature

Chemical compositions	Electrical conductivities	Refer.
$PrBaCo_2O_{5+d}$	1323 and 310 S/cm at 100 and 900 ºC	[13]
$SmBaCo_2O_{5+d}$	570 and 170 S/cm at 250 and 900 ºC	[13, 14]
$SmBa_{0.8}Ca_{0.2}Co_2O_{5+d}$	329.7 S/cm at 700 ºC	[15]
$SmBa_{0.5}Sr_{0.5}Co_2O_{5+d}$	1280 and 280 S/cm at 50 °C and 900 °C	[14]
$La_{0.6}Sr_{0.4}Co_{0.2}Fe_{0.8}O_3$	176 and 1867 S/cm at 300 and 800 ºC	[16, 17]
$La_{0.5}Ba_{0.5}Co_{0.9}Fe_{0.1}O_{3-d}$	800 S/cm at 227 ºC	[18]
$Pr_{0.4}Sr_{0.6}(Co_{0.2}Fe_{0.8})_{0.95}Mo_{0.05}O_{3-d}$	128.8 S/cm at 850 ºC	[19]
$GdBaCo_2O_{5+d}$	512 – 290 S/cm between 500 - 800 ºC	[20]
$Pr_{0.8}Sr_{0.2}FeO_3$	300 and 78 S/cm at 550 and 800 ºC	[21]
$Nd_{0.5}Sr_{0.5}Fe_{0.8}Co_{0.2}O_{3-d}$	124 S/cm at 700 ºC	[22]

Table 2. Abbreviation of dense microstructure samples

Chemical composition	Abbreviation
$SmBaCo_2O_{5+d}$ (SBCO)	D-A
$SmBa_{0.5}Sr_{0.5}Co_2O_{5+d}$ (SBSCO)	D-B

Table 3. Abbreviation of porous microstructural samples

Pt line	Cathode material	Abbreviation
Upper conductor (H)	$SmBaCo_2O_{5+d}$ (A)	H-AG
	$SmBa_{0.5}Sr_{0.5}Co_2O_{5+d}$ (B)	H-BG
Middle conductor (M)	A	M-AG
	B	M-BG
Lower conductor (L)	A	L-AG
	B	L-BG

Table 4. Calculated T_{max} from activation energies (listed in Table 4) of porous microstructural samples by applying current of 0.05 A

Atmosphere	**T_{max} (°C)**					
	H-AG	**H-BG**	**M-AG**	**M-BG**	**L-AG**	**L-BG**
Heating cycle in air	1281	1283	1595	1402	910	1213
Cooling cycle in air	1061	1334	3389	2197	1084	1365
Heating cycle in N_2	1518	1314	4649	2190	1477	1414
Cooling cycle in N_2	1432	1451	4113	3471	1054	1684

Table 5. Calculated T_{max} from activation energies of dense microstructural samples

Sample	**Atmosphere**	**Ea (eV)**	**T_{max} (^{o}C)**
D-A	Heating cycle in air	0.062	727
	Cooling cycle in air	0.066	760
	Heating cycle in N_2	0.080	928
D-B	Heating cycle in air	0.051	589
	Cooling cycle in air	0.053	613
	Heating cycle in N_2	0.079	915

Table 6. Calculated activation energies for the electrical conductivities at 400 ~ 650 ºC of all samples

Atmosphere	Current	Ea (eV)					
		H-AG	H-BG	M-AG	M-BG	L-AG	L-BG
Heating cycle in air	0.05	0.110	0.111	0.137	0.121	0.078	0.105
	0.075	0.111	0.109	0.138	0.121	0.078	0.104
	0.1	0.111	0.108	0.140	0.121	0.078	0.104
	0.3	0.112	0.108	0.140	0.121	0.078	0.104
Cooling cycle in air	0.05	0.091	0.115	0.292	0.189	0.094	0.118
	0.075	0.091	0.115	0.296	0.190	0.095	0.119
	0.1	0.091	0.116	0.294	0.193	0.096	0.120
	0.3	0.091	0.116	0.249	0.191	0.095	0.118
Heating cycle in N_2	0.01	0.133	0.114	0.414	0.179	0.129	0.119
	0.02	0.133	0.114	0.410	0.181	0.128	0.120
	0.03	0.132	0.113	0.406	0.183	0.128	0.121
	0.04	0.131	0.113	0.415	0.185	0.128	0.122
	0.05	0.131	0.113	0.401	0.189	0.127	0.122
Cooling cycle in N_2	0.01	0.099	0.125	0.362	0.325	0.091	0.148
	0.02	0.100	0.125	0.361	0.314	0.092	0.148
	0.03	0.102	0.125	0.361	0.311	0.092	0.146
	0.04	0.124	0.125	0.358	0.31	0.092	0.146
	0.05	0.123	0.125	0.354	0.299	0.091	0.145